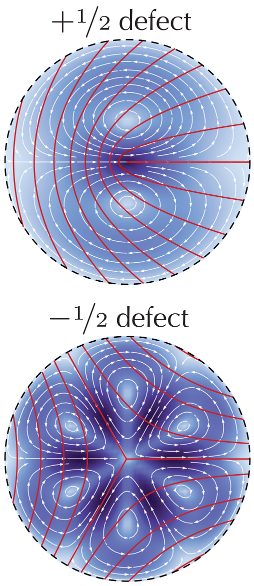

Figure 9.11. Illustration of director and induced flow fields around $+1/2$ and $-1/2$ defects in active nematics in a circular geometry, as determined by Giomi et al., 2014. The red lines show the director field, while the white arrows show the flow direction in the vicinity of the defect. The intensity of the blue background varies in proportion to the magnitude of the flow velocity. The asymmetric flow field induced by the $+1/2$ defect leads to self-propulsion of the defect. Image courtesy of Luca Giomi.[21]

While the term 'active turbulence' is commonly used, it is important to realize that the turbulence we studied for Newtonian fluids is a distinct phenomenon that occurs at high Reynolds numbers and involves scaling behavior due to energy transfer across decades of length scales, whereas the chaotic flows considered here occur at low Reynolds numbers.

9.5.3 Self-propulsion of topological defects

We have already encountered several examples of the fact that $+1/2$ topological defects in active nematics play an important role as drivers of the dynamics.[22] Because of the active flows generated by the motors, $+1/2$ and $-1/2$ defects exhibit very distinct behaviors: $+1/2$ defects inherently self-propel along their symmetry axis with some characteristic speed, while $-1/2$ defects are essentially stationary—they move only under the influence of external forces or gradients like those resulting from other nearby defects. This relation between defect motility and topological charge can be understood through symmetry arguments. In figure 9.11, the active flows around $\pm 1/2$ defects are plotted in white; a $+1/2$ defect has a well-defined polarity, leading to imbalanced active flows which propel the defect along its polarity axis. On the other hand, a $-1/2$ defect has no polarity. The active flows are balanced and there is no self-propulsion.

This symmetry argument can be backed up by a hydrodynamic analysis of active flows around isolated topological defects (subject of problem 9.7).[23] The flow $\vec{v}_0$ at the defect core is what propels a defect. For $\pm 1/2$ defects, the characteristic propulsion velocity is

$$\vec{v}_0 = \begin{cases} \frac{\alpha R}{4\eta}\hat{x} & s = +1/2, \\ 0 & s = -1/2. \end{cases} \tag{9.30}$$

The expression confirms that active stresses propel $+1/2$ defects along their symmetry axes, with the direction of motion set by the sign of α—active nematic media in which parallel filaments tend to contract (shorten) are called contractile and have $\alpha > 0$. When the filaments tend to extend, the medium is called extensile and $\alpha < 0$. Active flows do not propel $-1/2$ defects. Their motion is caused solely by elastic stresses coming from defect- or boundary-induced director distortions in the medium.

9.6 Active solids

We now consider the case of a solid composed of active components. Once again, we have to reevaluate our passive continuum model now that conservation of energy, linear momentum, and angular momentum constraints are lifted. This modifies the relation between continuum force density $f_i(\vec{r})$ and deformations parameterized by the displacement field $u_i(\vec{r})$, where the subscript i labels spatial directions. A gradient expansion of the continuum force density then takes the general form

$$f_i = f_i^0 + A_{ik}u_k + B_{ijk}\partial_j u_k + K_{ijkl}\partial_j\partial_l u_k + \cdots, \tag{9.31}$$

where f^0 is a constant force independent of deformation, K_{ijkl} is the stiffness tensor containing the elastic moduli, and A_{ij} and B_{ijk} are tensor coefficients that stipulate respectively the dependence of the force on particle displacements (e.g., pinning to a substrate) and displacement gradients. The latter can arise from an effective violation of Newton's third law (as discussed in the next section). As a result, the familiar second derivative term due to elasticity is no longer the leading contribution. In addition, we shall see that the usual symmetries of the stiffness tensor are no longer valid when energy is not conserved. These new terms are responsible for the phenomena that we shall encounter, and they range from transverse and nonreciprocal responses to self-sustained energy cycles and active waves.

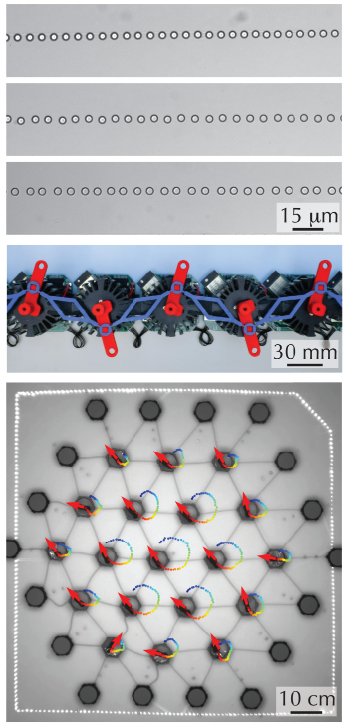

Figure 9.12. Top: quasi-one-dimensional solids made of oil droplets in water in a microfluidic channel in the experiments by Beatus et al., 2006. The droplets are generated on the left (not in view) and advected by the water to the right. Because of the underlying water flow, the force exerted by a droplet on its left-hand neighbor is different from the force on its right-hand one—interactions are not reciprocal. This leads to asymmetric wave propagation with dispersion $\omega(-q) \neq \omega(q)$ and to complex instabilities (two bottom images). Image courtesy of Tsevi Beatus and Roy Bar-Ziv. Middle: mechanical metamaterial made of robotic units. Programmable sensors and motors are used to implement nonreciprocal couplings between neighboring units; see Ghatak et al., 2020. This leads to unidirectional (nonreciprocal) wave propagation. Image courtesy of Corentin Coulais.[24] Bottom: active solid composed of polar active agents embedded in an elastic lattice in experiments by Baconnier et al., 2022. Selective and collective actuation (limit cycle behavior) emerge in this system from the interplay between activity and elasticity. Image courtesy of Paul Baconnier and Olivier Dauchot.

9.6.1 Moving and self-propelled solids

In the top and middle of figure 9.12, we show two active solids in which energy injection at the microscopic scale modifies the elastic response. The top panel shows a quasi-one-dimensional solid made of oil droplets generated on the left of a microfluidic channel filled with water, and pushed to the right by the water flow. The asymmetry of the driving field leads to nonreciprocal forces between the droplets: the force exerted by a droplet on its left-hand neighbor is different from the force on its right-hand neighbor. This is an effective violation of Newton's third law of action and reaction as well as a breaking of mirror symmetry ($x \to -x$). Similar nonreciprocal interactions can be engineered in robotic metamaterials such as the one shown in the middle panel, where they arise from motors controlled by sensors.

As a minimal model for these systems, we consider a one-dimensional solid described by a scalar deformation field $u(t, x)$ whose dynamics is described by

$$\gamma\partial_t u = \beta\partial_x u + \kappa\partial_x^2 u. \tag{9.32}$$

Note that we can think of (9.32) as obtained from (2.25) in the overdamped limit.

Here, κ is the shear modulus, β is a parameter absent from standard elasticity that accounts for nonreciprocal forces that break mirror symmetry, and γ plays the role of a friction coefficient. For simplicity, we set $\gamma = 1$. By performing a Fourier transform, we obtain the following dispersion relation

$$\sigma - i\omega = -\kappa q^2 + i\beta q, \tag{9.33}$$

where σ is the growth rate of small disturbances and ω is their vibration frequency. We see that $\omega(q) = -\beta q = -\omega(-q)$. This dispersion relation can be contrasted to that of normal elastic waves in an underdamped solid (ruled by the equation $\partial_t^2 u = \kappa \partial_x^2 u$) for which $\omega(q) = \sqrt{\kappa}|q| = \omega(-q)$ (see section 2.6).

Continuing with figure 9.12, bottom panel shows another type of active solid, composed of moving objects. Here, however, self-propelled particles (similar to the ones we already encountered in section 9.2) occupy nodes of a two-dimensional lattice made of elastic medium. For describing this system at the continuum level, it is therefore natural to combine an order parameter describing deformations $u_i(\vec{r}, t)$ (as in elasticity; see chapter 2) with an order parameter describing the polarization $\vec{p}(\vec{r}, t)$ of the particles (as in flocking; see section 9.2). This hydrodynamic theory allows us to predict the onset of the collective rotational actuation arising from the combination of self-propulsion and pinning of the system at the edge.

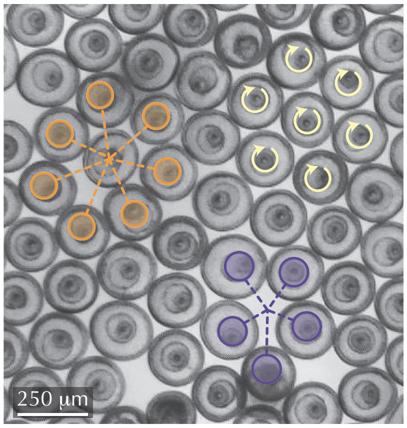

Figure 9.13. Starfish embryos which self-organize into living chiral crystals perform a global collective rotation. From Tan et al., 2022. The image shows a magnified snapshot of the lattice showing topological defects called disclinations. A fivefold defect in the lattice is marked in purple, and a sevenfold defect in orange. The yellow arrows indicate the spinning direction of the embryos. Image courtesy of Nikta Fakhri. Measurements of odd-elastic moduli for this system have been reported by Tan et al., 2022 by comparing experimental measurements of the strain field around defects with theoretical predictions by Braverman et al., 2021.

9.6.2 Odd elasticity

Figure 9.13 illustrates an in vitro biological realization of chiral crystals of rotating embryos in which anomalous mechanical behavior has been reported and attributed to an active generalization of elasticity known as odd elasticity. Nonliving matter examples of active robotic metamaterials are shown in figure 9.14. Although we will not study these systems in detail, our analysis of odd elasticity applies to them. Elasticity usually assumes conservation of energy. Odd elasticity is a generalization of traditional elasticity with this assumption lifted—forces in active solids are typically nonconservative, and hence cannot be derived from a potential.

Let us start with the general constitutive relation (compare the discussion following equation (2.3))

$$\sigma_{ij} = \sigma_{ij}^{\text{pre}} + K_{ijkl}\, e_{kl}. \tag{9.34}$$

Here, σ_{ij} is the stress tensor, $e_{kl} \equiv \partial_l v_k$ is the (unsymmetrized) deformation gradient tensor, and σ_{ij}^{pre} are stresses present even when the solid is undeformed (they are called prestresses). The tensor K_{ijkl} contains elastic moduli. If all forces are conservative, then the stress tensor can be written as the derivative

$$\sigma_{ij} = \frac{\partial \mathcal{F}}{\partial e_{ij}} \tag{9.35}$$

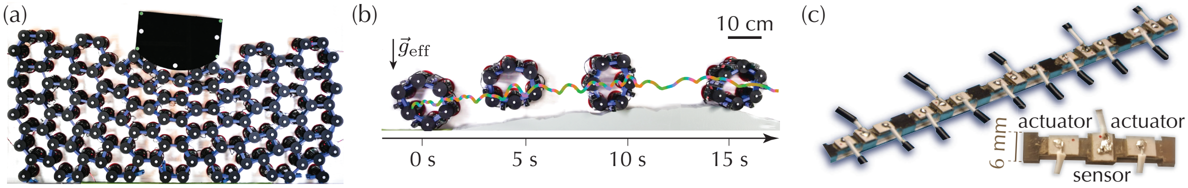

Figure 9.14. Active solids with odd elasticity are relevant to robotic metamaterials, as the energy cycles can power robotic functionalities such as propulsion (see also chapter 10). The figure shows three examples. (a) A robotic metamaterial with active hinges; each one of the elements is a minimal robot that is able to sense the behavior of its neighbors and act consequently. This type of system exhibits anomalous impact response: a bullet hitting the odd-elastic wall is deflected at an angle controlled by the sign of the odd modulus $K^{\rm o}$. From Brandenbourger et al., 2021. (b) Four successive snapshots illustrating locomotion of a chiral robotic element with nonlinear work cycle. The elements consist of chiral elements connected with passive bands (blue) providing bending stiffness, and with sensors providing feedback. From Brandenbourger et al., 2021. Images a and b courtesy of Martin Brandenbourger. (c) A freestanding active metabeam with piezoelectric elements and electronic feed-forward control that displays odd elasticity. This results in a direction-dependent bending modulus and unidirectional wave amplification. Adapted from Y. Chen et al., 2021.

of some strain energy density

$$\mathcal{F} = \frac{1}{2} C_{ijkl} e_{ij} e_{kl}, \tag{9.36}$$

so that $\sigma_{ij} = \frac{1}{2}\left(C_{ijkl} + C_{klij}\right) e_{kl}$ and therefore

$$K_{ijkl} = K_{klij}. \tag{9.37}$$

The symmetry $K_{ijkl} = K_{klij}$ of the stiffness tensor is known as Maxwell-Betti reciprocity.

Odd elasticity emerges from nonconservative forces which cannot be represented as a derivative of an energy. Now, in general the elastic stiffness tensor can be decomposed into even and odd parts,

$$K_{ijkl} = K^{\rm e}_{ijkl} + K^{\rm o}_{ijkl}, \tag{9.38}$$

with

$$K^{\rm e}_{ijkl} = K^{\rm e}_{klij} \qquad \text{and} \qquad K^{\rm o}_{ijkl} = -K^{\rm o}_{klij}. \tag{9.39}$$

We refer you to Fruchart et al., 2023 for an introduction to odd elasticity and to Scheibner et al., 2020 for a more detailed discussion.

The tensor $K^{\rm e}_{ijkl}$ contains the usual (even) moduli arising from conservative forces, while $K^{\rm o}_{ijkl}$ holds odd-elastic moduli arising from nonconservative forces. Odd elasticity results from the influence of the additional elastic moduli contained in $K^{\rm o}_{ijkl}$.

We will focus on odd elasticity in the special case of a two-dimensional solid. In such a material, the modulus tensor K_{ijkl} has 16 independent components while e_{kl} has four components. Though e_{kl} is a rank 2 tensor, we can represent it as a column vector e_α using as a basis the matrices given in (9.40). These correspond to the four modes of deformation, namely dilation, rotation, and two different shears. They form a complete basis, which allows us to write any matrix e_{ij} as a column vector e_α such that $e_{ij} = \sum_\alpha e_\alpha \left(\tau_\alpha\right)_{ij}$.

The four real basis matrices are given by

$$\begin{aligned} \tau_0 &= \begin{pmatrix} 1 & 0 \\ 0 & 1 \end{pmatrix}, \quad \tau_1 = \begin{pmatrix} 0 & 1 \\ -1 & 0 \end{pmatrix}, \\ \tau_2 &= \begin{pmatrix} 1 & 0 \\ 0 & -1 \end{pmatrix}, \quad \tau_3 = \begin{pmatrix} 0 & 1 \\ 1 & 0 \end{pmatrix}. \end{aligned} \tag{9.40}$$

When viewed as vectors in the space of 2×2 matrices, these matrices are normed and orthogonal to each other. One can show (see problem 9.8) that they obey the identity

$$\frac{1}{2} \sum_{ij} (\tau_\alpha)_{ij} (\tau_\beta)_{ij} = \delta_{\alpha\beta}. \tag{9.41}$$

Any 2×2 matrix X can uniquely be written as $X = x_\alpha \tau_\alpha$. In this section, the components of quantities with respect to this basis are indicated with Greek indices, while the spatial components of matrices (tensors) are indicated with Roman indices.

We can similarly write the stress components as a column vector $\sigma_{ij} = \sigma_\gamma \left(\tau_\gamma\right)_{ij}$, where the basis matrices now correspond to pressure, torque, and two shear stresses. The elastic moduli tensor

Table 9.1. Irreducible components of rank 2 tensors in two dimensions. A pure shear (rate) corresponds to a (rate of) change in shape without a change in volume or orientation. Shear 1 describes a horizontal elongation and vertical compression while shear 2 describes elongation along the 45° direction and compression along the −45° direction. They are mathematically orthogonal. We note that $\dot{e}_0 = \nabla \cdot v$ and $\dot{e}_1 = \omega$ is vorticity. The stresses are the conjugate forces to these deformations, and they have similar interpretations. In particular, σ_0 includes pressure and the antisymmetric stress is σ_1. Adapted from Fruchart et al., 2023.

deformation	deformation rate	stress	geometric meaning
$e_0 = \; = \partial_x u_x + \partial_y u_y$	$\dot{e}_0 = \; = \partial_x v_x + \partial_y v_y$	$\sigma_0 = \; = [\sigma_{xx} + \sigma_{yy}]/2$	isotropic area change
$e_1 = \; = \partial_x u_y - \partial_y u_x$	$\dot{e}_1 = \; = \partial_x v_y - \partial_y v_x$	$\sigma_1 = \; = [\sigma_{yx} - \sigma_{xy}]/2$	rotation
$e_2 = \; = \partial_x u_x - \partial_y u_y$	$\dot{e}_2 = \; = \partial_x v_x - \partial_y v_y$	$\sigma_2 = \; = [\sigma_{xx} - \sigma_{yy}]/2$	pure shear 1
$e_3 = \; = \partial_x u_y + \partial_y u_x$	$\dot{e}_3 = \; = \partial_x v_y + \partial_y v_x$	$\sigma_3 = \; = [\sigma_{xy} + \sigma_{yx}]/2$	pure shear 2

becomes a matrix in this basis, allowing the constitutive relation (9.34) to be written compactly as (see problem 9.8 for the intermediate steps and more details)

$$\sigma_\alpha = K_{\alpha\beta} e_\beta, \tag{9.42}$$

where

$$K_{\alpha\beta} = \frac{1}{2} (\tau_\alpha)_{ij} \, K_{ijkl} \, (\tau_\beta)_{kl}. \tag{9.43}$$

Using the graphical notation summarized in table 9.1, the column vectors for stress and strain read

$$\sigma_\alpha = \begin{pmatrix} \\ \\ \\ \end{pmatrix} \qquad \text{and} \qquad e_\beta = \begin{pmatrix} \\ \\ \\ \end{pmatrix}, \tag{9.44}$$

In addition to the work on spinning embryos, see Biliiign et al., 2021 for a study of spinning colloids, where experimental behaviors compatible with odd elasticity are reported. See also Shankar and Mahadevan, 2022 and Zahalak, 1996 for a discussion of anisotropic odd elasticity in the context of muscles.

where similar to the components of σ_α the components of e_β represent dilation, rotation, and the two shears (see problem 9.8).

Assuming that the material under consideration is invariant under rotations, the most general matrix $K_{\alpha\beta}$ then reads

$$\underset{\sigma_\alpha}{\begin{pmatrix} \\ \\ \\ \end{pmatrix}} = \underset{\sigma_\alpha^{(\mathrm{pre})}}{\begin{pmatrix} -p^{(\mathrm{pre})} \\ -\tau^{(\mathrm{pre})} \\ 0 \\ 0 \end{pmatrix}} + \underset{K_{\alpha\beta}}{\begin{pmatrix} B & \Lambda & 0 & 0 \\ A & \Gamma & 0 & 0 \\ 0 & 0 & \mu & K^o \\ 0 & 0 & -K^o & \mu \end{pmatrix}} \underset{e_\beta}{\begin{pmatrix} \\ \\ \\ \end{pmatrix}}. \tag{9.45}$$

We refer you to Poncet and Bartolo, 2022 for a systematic treatment of active solids with effective violations of Newton's third law and to Baek et al., 2018; Chajwa et al., 2020; Ivlev et al., 2015; Meredith et al., 2020; Saha et al., 2014; and Soto and Golestanian, 2014 for examples of systems in which such forces are generated.

In this equation, the prestresses include a hydrostatic pressure p^{pre} and a hydrostatic torque τ^{pre} present even when the system is undeformed. The hydrostatic torque is therefore a zeroth order effect that drives a large part of the phenomenology of systems with broken mirror symmetry. The coefficients B and μ are the familiar compression and shear moduli from passive elasticity.[25] One often assumes that solid-body rotations do not induce stresses, implying $\Lambda = \Gamma = 0$. This assumption can, however, be violated, for instance, when the solid is on a substrate.

The remaining terms A and K^o are odd-elastic moduli. They are allowed when the symmetry constraint $K_{ijkl} = K_{klij}$ (equivalently, $K_{\alpha\beta} = K_{\beta\alpha}$) is lifted. A represents a coupling of dilation to torques while K^o describes a shear stress response which is rotated with respect to an applied strain.

As a result of these new moduli, the work done on the system is no longer a state function but in fact depends on the path taken in strain space. If odd elasticity is present, work can be extracted or lost from the system by performing quasi-static strain cycles. Elastic forces are given by $f_i = \partial_j \sigma_{ij}$, so the power per unit area exerted by elastic forces when the solid is deformed is $f_i \dot{u}_i$. Consider now a cyclic deformation $u_i(t) = u_i(t+T)$ imposed from the outside. The work done over one cycle of deformation is then

$$\Delta W = \int \mathrm{d}t f_i \dot{u}_i = -\oint \mathrm{d}e_{ij}\sigma_{ij} = -\oint \mathrm{d}e_{ij} K^o_{ijkl} e_{kl} \neq 0. \tag{9.46}$$

To see that this quantity is in general not zero, let us take the dilation-torque coupling $A = 0$. The work done over some cyclic path in strain space is then

$$\Delta W = \oint \mathrm{d}e_{ij}\sigma_{ij} = \oint \mathrm{d}e_{\beta}\sigma_{\beta} = \int \mathrm{d}^2 S\, \epsilon_{\alpha\beta} \frac{\partial \sigma_\beta}{\partial e_\alpha}, \tag{9.47}$$

where in the rightmost term the integral is over the area enclosed by the path in strain space and $\underline{\epsilon}$ is the two-dimensional Levi-Civita tensor (see equation (2.124)). Only the odd components $K_{\alpha\beta} = K^o \epsilon_{\alpha\beta}$ will remain, leading to

$$\Delta W = \int \mathrm{d}^2 S\, \epsilon_{\alpha\beta}\epsilon_{\alpha\beta} K^o = 2K^o \times \text{Area}. \tag{9.48}$$

Thus, the work extracted from an odd-elastic engine is proportional to the odd-elastic modulus and the area of the cycle in strain space. We can visualize this using an example of a microscopic model with odd-elastic bonds, depicted in figure 9.15. The force law of the linear spring with odd elasticity is

$$\vec{f} = -(k\hat{r} + k^o\hat{\phi})\delta r, \tag{9.49}$$

where we use polar coordinates, so that $\hat{r}$ is the unit vector pointing along the spring, $\hat{\phi}$ the unit vector orthogonal to $\hat{r}$, and δr the spring extension, while k^o is the odd and k the regular microscopic spring constant.

In problem 9.9, we calculate the net work done over the cycle shown in figure 9.15 directly, and we confirm that it is proportional

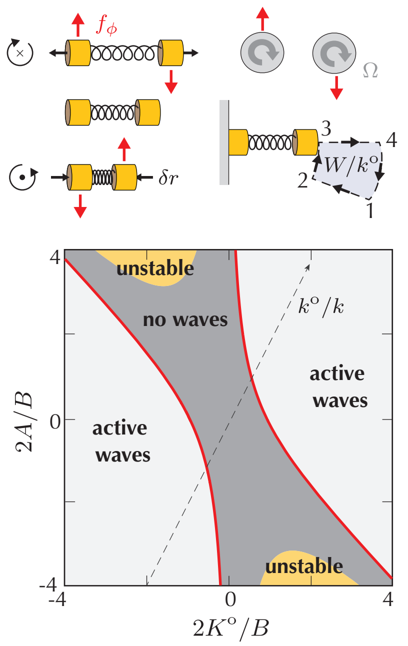

Figure 9.15. Upper panel right: schematic illustration of two disks of diameter d, separated by a distance r and spinning in a fluid at angular speed Ω. They experience non-central hydrodynamic forces (i.e., forces that have a component f_ϕ transverse to the vector joining the centers of the particles). Upper panel left: A microscopic odd-elastic spring. In addition to the standard compression/extension force, the spring exerts a force $f_\phi = k^o \delta r$ transverse to its radial displacement δr. Bottom right of upper panel: an odd-elastic energy cycle. The spring is stretched through the path shown and the work is proportional to the area of the path times k^o. Lower panel: schematic phase diagram of the odd-elastic media as a function of the odd moduli A and K^o normalized by the bulk modulus B. The red lines indicate the transition between an overdamped solid without wave propagation and active waves (it coincides with a line of exceptional points; see text). The dashed line represents a trajectory of increasing odd microscopic spring constant k^o. Note that the medium becomes unstable in the yellow areas. Adapted from Scheibner et al., 2020.

to both k^{o} and the area enclosed by the path. This ability to extract work enables self-sustained waves powered by odd-elastic energy cycles in overdamped media that contain the noncentral springs. An experimentally viable way of generating noncentral interaction forces is by having colloidal particles, swimming algae, or embryos that constantly spin in a fluid so that they experience friction-like transverse forces. In fact, it is possible to obtain explicit formulas for the odd moduli by coarse-graining these microscopic forces.[26]

For a study of the hydrodynamics of swimming algae we refer you to Drescher et al., 2009.

9.6.3 Odd elastodynamics

We now discuss the effect of odd elasticity on dynamics. As we shall see, odd elasticity can lead to active waves in overdamped systems and even to instabilities. For overdamped systems, the dynamics of the displacement field can be described by taking

An example of transverse hydrodynamic interaction is the so-called lubrication force $f_\phi \propto \Omega \log\left(\frac{r-d}{d}\right)$ between two disks whose diameter is equal to d, at distance r from each other, spinning with fixed angular speed Ω (Happel and H. Brenner, 1982). Note, however, that these hydrodynamic forces are not pairwise additive.

$$\gamma \partial_t u_i = f_i = \partial_j \sigma_{ij}, \tag{9.50}$$

where γ is a friction coefficient. Using the constitutive relation in equation (9.45) along with table 9.1, we find that the odd-elastodynamics equations explicitly read

$$\gamma \partial_t \vec{u} = B \vec{\nabla}(\vec{\nabla}\cdot\vec{u}) + \mu \Delta \vec{u} + K^{\mathrm{o}} \underline{\epsilon} \cdot \Delta \vec{u} - A \underline{\epsilon} \cdot \vec{\nabla}(\vec{\nabla}\cdot\vec{u}). \tag{9.51}$$

As in (9.47), $\underline{\epsilon}$ is the Levi-Civita tensor.

Performing a Fourier transform of equation (9.51), we find

$$i\gamma\omega \begin{pmatrix} u_\parallel \\ u_\perp \end{pmatrix} = q^2 \begin{pmatrix} B+\mu & K^{\mathrm{o}} \\ -K^{\mathrm{o}}+A & \mu \end{pmatrix} \begin{pmatrix} u_\parallel \\ u_\perp \end{pmatrix}, \tag{9.52}$$

in which we have defined the longitudinal $u_\parallel = \hat{q}\cdot u$ and transverse $\vec{u}_\perp = \vec{u} - u_\parallel \hat{q}$ components of the displacement. In an overdamped system, passive elastodynamics ($A = K^{\mathrm{o}} = 0$) is diffusive: $\omega = -iq^2 \frac{B+\mu}{\gamma}$ and $\omega = -iq^2 \frac{\mu}{\gamma}$ (with our conventions, a negative imaginary frequency implies that a wave is attenuated). In the case of an overdamped odd-elastic solid with $A, K^{\mathrm{o}} \neq 0$, we obtain

In rotating Rayleigh-Bénard convection, the fluid is put under rotation, leading to Coriolis forces (see chapter 8). The relaxation of the pattern is then described by an equation of motion formally identical to that of odd elastodynamics, even if the interpretation in terms of stress does not carry through; see Fruchart et al., 2023 and references therein.

$$\omega = -iq^2 \frac{B/2 + \mu \pm \sqrt{(B/2)^2 - K^{\mathrm{o}}(K^{\mathrm{o}} - A)}}{\gamma}. \tag{9.53}$$

When $K^{\mathrm{o}}(K^{\mathrm{o}} - A) > (B/2)^2$, the frequency has a real part: there are oscillations even though the system is overdamped. The transition between exponential relaxation and damped oscillations, marked by an exceptional point of the matrix in equation (9.52), is the point where the matrix is not diagonalizable (red lines in figure 9.15), in a similar way as in a damped harmonic oscillator. The system can even become unstable (yellow region in figure 9.15) when the imaginary part of the frequency becomes positive.

Experimental observations of such elastic waves have been reported in the systems shown in figure 9.14.

In this case, linear elasticity cannot accurately describe the system and nonlinearities have to be considered.

9.7 Chiral active fluids

Consider an active granular fluid whose particles are constantly spinning in a plane. In a passive granular system, the particles lose energy in collisions through friction, while in an active one, the particles can gain energy when their rotation speed is reset after a collision by microscopic torques or external fields. Active matter whose particles are all spinning in the same direction is known as a chiral active fluid. We already showed a couple of examples of chiral active fluids in figure 9.14 (collections of robots) and figure 9.13 (spinning embryos), but chiral active behavior has also been observed in magnetic colloids; see figure 9.16. In all these systems there is a central force that models a soft repulsion between particles and a noncentral force that captures interparticle friction. In addition to this interaction force, each particle experiences an active torque which tends to maintain a constant angular velocity. This active torque imparts a fixed chirality to the system. The macroscopic effects of these microscopic ingredients can be captured by the hydrodynamic approach summarized below.

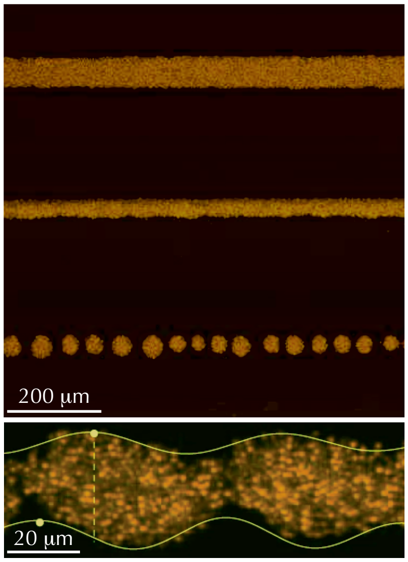

Figure 9.16. Layers of a chiral active fluid consisting of spinning colloidal magnets. The particles are made to spin in a magenetic field. Upper panel: various snapshots of layers of varying thickness. Below a thickness of 32 μm the layers exhibit a hydrodynamic instability. Lower panel: a chiral fluid strip approaching instability. Experiments on this instability allow us to test minimal hydrodynamic models of chiral fluids in detail. Adapted from Soni et al., 2019.

9.7.1 Hydrodynamics of self-spinning particles

The Navier-Stokes equations that we introduced in chapter 1 describe the conservation of mass and linear momentum (and possibly of energy). In order to describe a collection of spinning objects, one has to also consider the angular momentum of the particles at the continuum level. For identical particles, this can be done by introducing the angular velocity field $\vec{\Omega}(\vec{r}, t)$ as the coarse-grained version of the spinning speed of individual particles, very much as the velocity field $\vec{v}(\vec{r}, t)$ is a coarse-grained version of the translation speeds of individual particles.[27]

Even in passive fluids, it is sometimes necessary to add a continuum equation to describe the conservation of angular momentum. This equation is in principle required as soon as the particles are not point-like, and even more so if they are not spherical. However, it is often the case that the angular velocity field relaxes more quickly than other fields, and it can therefore be ignored or eliminated.

For concreteness, we consider a two-dimensional fluid of spinners, where the angular velocity field is a pseudoscalar $\Omega(\vec{r}, t)$. The resulting continuum equations read

$$
\begin{aligned}
(\partial_t + \vec{v}\cdot\vec{\nabla})\rho &= -\rho\vec{\nabla}\cdot\vec{v}, \\
\rho(\partial_t + \vec{v}\cdot\vec{\nabla})\vec{v} &= \vec{\nabla}\cdot\underline{\sigma} + \vec{f}_{\text{vol}}, \\
I(\partial_t + \vec{v}\cdot\vec{\nabla})\Omega &= \tau + \epsilon_{ij}\sigma_{ij} - \Gamma_\Omega\Omega + \eta_\Omega\nabla^2\Omega,
\end{aligned}
\tag{9.54}
$$

where $\omega = (\vec{\nabla}\times\vec{v})_z$ is the vorticity and $\vec{f}_{\text{vol}}$ are body forces, and τ are body torques. Besides, Γ_Ω is a phenomenological damping term describing the damping of the spinning, while Γ describes the coupling between spinning and vorticity, and η_Ω is a rotational viscosity. Finally, the stress is

$$\sigma_{ij} = \epsilon_{ij}\frac{\Gamma}{2}(\Omega - \omega) - P\delta_{ij} + \eta_{ijkl}\partial_l v_k + \frac{I\Omega}{2}\left(\partial_i \epsilon_{jl} v_l + \epsilon_{il}\partial_l v_j\right). \tag{9.55}$$

While these equations have several moving parts, note that the angular velocity field and the velocity field are coupled by the stress σ_{ij}. When the driving performed by external torques τ is strong enough, a steady state with almost uniform and almost constant angular velocity $\Omega \approx \tau/\Gamma_\Omega$ can be achieved. In this regime, the angular velocity field can be integrated out to obtain an effective hydrodynamic equation for the velocity and the density fields. At this level, the main effect of a maintained rotation of the particles is the appearance of additional terms in the hydrodynamic response—in the viscosity tensor—as we discuss in the next section.

Outside of the regime, where Ω is approximately uniform and constant, more complex behaviors can occur, where the full continuum equations (9.54) are needed.

9.7.2 Odd viscosity

See Fruchart et al., 2023 for an introduction to odd viscosity.

The evolution of the velocity field $\vec{v}$ of the chiral active fluid is described by the Navier-Stokes equation for an incompressible fluid,

$$\rho(\partial_t + \vec{v}\cdot\vec{\nabla})\vec{v} = \vec{\nabla}\cdot\underline{\sigma} + \vec{f}_{\text{vol}}, \tag{9.56}$$

where the term on the left is the material derivative (1.1), $\underline{\sigma}$ is the stress tensor, f_{vol} are external body forces, and $\rho = nm$ is the mass density (n is the number density), which is taken as constant (see section 1.9). The stress tensor $\underline{\sigma}$ in equation (9.56) is composed of a reversible part $\underline{\sigma}^{\text{ss}}$ (the pressure for ordinary fluids; see section 1.5), and a dissipative or viscous part $\underline{\sigma}^{\text{vis}}$ that describes surface forces between fluid layers that arise in response to velocity gradients.

The viscous stress is given by $\sigma_{ij}^{\text{vis}} = \eta_{ijkl}\,\partial_l v_k$, where η_{ijkl} is the viscosity tensor of the fluid. In the same way as in section 9.6.2, we decompose the viscosity tensor

Just as in section 9.6.2 on odd elasticity, it is convenient to express σ_{ij}^{vis} and the unsymmetrized shear rate $\dot{e}_{kl} \equiv \partial_l v_k$ as column vectors $\sigma_\alpha^{\text{vis}}$ and $\dot{e}_\beta$ using as basis the matrices introduced in equation (9.40). Then η_{ijkl} can be represented as a matrix $\eta_{\alpha\beta}$.

$$\eta_{ijk\ell} = \eta^{\text{e}}_{ijk\ell} + \eta^{\text{o}}_{ijk\ell} \tag{9.57}$$

into symmetric (even) $\eta^{\text{e}}_{ijk\ell} = \eta^{\text{e}}_{k\ell ij}$ and antisymmetric (odd) $\eta^{\text{o}}_{ijk\ell} = -\eta^{\text{o}}_{k\ell ij}$ parts. Odd viscosities are contained in $\eta^{\text{o}}_{ijk\ell}$, i.e., they are those that violate the symmetry $\eta_{ijk\ell} = \eta_{k\ell ij}$ (or, equivalently, $\eta_{\alpha\beta} = \eta_{\beta\alpha}$; see the margin note next to (9.57)).

Usual viscosities are dissipative. The rate of loss of mechanical energy by viscous dissipation per unit volume is[28]

$$\dot{w} = \sigma^{\mathrm{vis}}_{ij}\partial_j v_i = \eta_{ijk\ell}(\partial_j v_i)(\partial_\ell v_k) = \eta^{\mathrm{e}}_{ijk\ell}(\partial_j v_i)(\partial_\ell v_k). \tag{9.58}$$

Therefore, only the symmetric part of the viscosity tensor contributes to viscous dissipation. Odd viscosities correspond to the non-dissipative part of the viscosity tensor.

In the context of non-equilibrium thermodynamics, the symmetry $\eta_{ijk\ell} = \eta_{k\ell ij}$ of the viscosity tensor is known as Onsager reciprocity; see section 1.5.

As an example, let us consider the constitutive relation for rotation invariant two-dimensional fluids,

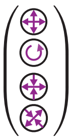

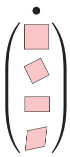

$$\sigma_\alpha = \underbrace{\begin{pmatrix} -p \\ -\tau \\ 0 \\ 0 \end{pmatrix}}_{\sigma^{\mathrm{h}}_\alpha} + \underbrace{\begin{pmatrix} \zeta & \eta^{\mathrm{B}} & 0 & 0 \\ \eta^{\mathrm{A}} & \eta^{\mathrm{R}} & 0 & 0 \\ 0 & 0 & \eta & \eta^{\mathrm{o}} \\ 0 & 0 & -\eta^{\mathrm{o}} & \eta \end{pmatrix}}_{\eta_{\alpha\beta}} \dot{e}_\beta . \tag{9.59}$$

See table 9.1 for the deformation rates and stresses σ_α. The viscosity matrix includes the standard bulk ζ and shear η viscosity coefficients, and several new ones which are allowed due to broken time-reversal and parity (i.e., mirror) symmetry. The *odd viscosity* η^{o} couples shear strains and stresses, and additional parity-violating viscosities η^{A} and η^{B} couple compression and rotation.

Odd viscosity has been measured in a number of systems, including chiral fluids composed of self-spinning colloids (Soni et al., 2019)—see figure 9.16—as well as magnetized polyatomic gases—see Beenakker and McCourt, 1970 and references therein (table 2)—and electrons in the presence of an external magnetic field—see Berdyugin et al., 2019.

Using the constitutive relation in equation (9.59) along with table 9.1, we find that the full Navier-Stokes equation reads

$$\begin{aligned} \rho \mathrm{d}_t \vec{v} = {} & \vec{\nabla}\cdot\underline{\sigma}^{\mathrm{h}} + \zeta\,\vec{\nabla}(\vec{\nabla}\cdot\vec{v}) + \eta\,\Delta\vec{v} + \eta^{\mathrm{o}}\,\underline{\epsilon}\cdot\Delta\vec{v} \\ & - \eta^{\mathrm{A}}\,\underline{\epsilon}\cdot\vec{\nabla}(\vec{\nabla}\cdot\vec{v}) + \eta^{\mathrm{B}}\,\vec{\nabla}(\vec{\nabla}\times\vec{v}) - \eta^{\mathrm{R}}\,\underline{\epsilon}\cdot\vec{\nabla}(\vec{\nabla}\times\vec{v}), \end{aligned} \tag{9.60}$$

in which $\underline{\sigma}^{\mathrm{h}}$ is the hydrostatic stress tensor $(\vec{\nabla}\times\vec{v})_z = \epsilon_{ij}\partial_i v_j$ in two dimensions, and d_t denotes the material derivative (1.2).

The appearance of odd viscosity can be understood from the more general hydrodynamics discussed in section 9.7.1 by focusing on the last term in the stress equation (9.55). Assuming incompressibility ($\vec{\nabla}\cdot\vec{v} = 0$) and using the identity $\vec{\nabla}\omega = \underline{\epsilon}\cdot\nabla^2\vec{v}$ for incompressible two-dimensional fluids, one can show that

$$\partial_j\sigma_{ij} = \frac{I\Omega}{2}\partial_j\left(\epsilon_{jl}\partial_i v_l + \epsilon_{il}\partial_l v_j\right) + \cdots = \frac{I\Omega}{2}\epsilon_{ij}\nabla^2 v_j + \cdots . \tag{9.61}$$

Comparison between equations (9.60) and (9.61) shows that this system exhibits odd viscosity, with

$$\eta^{\mathrm{o}} = \frac{I\Omega}{2}. \tag{9.62}$$

The relation between odd viscosity and microscopic violations of mirror symmetry can be quantified in certain microscopic models. For each collision, one computes the twisting angle $\theta \equiv \mathrm{angle}(\vec{v}, \Delta\vec{v})$ between the initial velocity $\vec{v}$ and the change in velocity during the collision $\Delta\vec{v}$. The ratio η^{o}/η is then proportional to $\langle\theta\rangle$, the average twisting over the ensemble of all particles (M. Han et al., 2021).

The odd viscosity is a hydrodynamic manifestation of the chiral collisions in a microscopic model. When two self-spinning particles collide, their outgoing velocities will be rotated compared to the incoming ones in a manner set by their spinning direction. Odd viscosity is not related to energy dissipation and, unlike standard (even) viscosity, cannot be derived from an entropy production rate equation, very much as an odd-elastic coefficient cannot be derived from variations of an elastic potential energy.

Hydrodynamic theories of active fluids capture several striking phenomena observed in experiments, including the instability shown in figure 9.16.

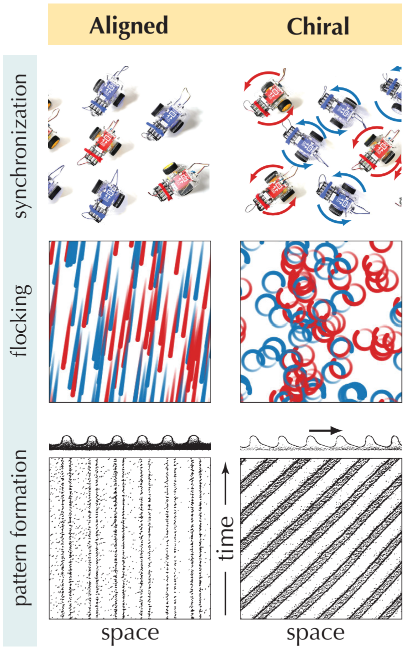

Figure 9.17. Nonreciprocal interactions between two species, R (Red) and B (Blue), induce a phase transition from static alignment to a chiral motion that spontaneously breaks parity. Top: nonreciprocal synchronization. Angular variables with nonreciprocal interactions drawn as robots spontaneously rotate either clockwise or counterclockwise, despite no average natural frequency ($\omega_m = 0$ in equation (9.63)). Middle row: non-reciprocal flocking. Self-propelled particles run in circles despite the absence of external torques. Bottom: space-time plots of an example of pattern formation with nonreciprocal interaction. A one-dimensional stationary pattern starts traveling, either to the left or to the right as in the chiral case, when nonreciprocal interactions are turned on. The figure represents an experimental observation of a moving oil-air interface (so-called viscous fingering). Adapted and reproduced with permission from Fruchart et al., 2021.[29]

9.8 Nonreciprocal phase transitions

Non-equilibrium systems are typically modeled by stochastic processes that violate detailed balance. As a result, the steady states of these systems are characterized by nonvanishing probability currents between microstates, and they exhibit entropy production. A simple example is a system composed of three states with cyclic clockwise transition rates. The steady state is reached when the probabilities of being in each state are equal. This system is not at equilibrium even if it possesses a Boltzmann distribution with constant energy because it does not obey detailed balance. Similarly, physical systems with absorbing states—states out of which transitions have zero probability—clearly violate detailed balance.[30] Flocking states are a non-equilibrium example of such behavior. Nonreciprocal phase transitions describe the transitions from and to these non-equilibrium steady states.

When we discussed the flocking transition in terms of the Toner-Tu theory of section 9.2.3, we associated the transition with a pitchfork bifurcation arising from minimizing a quartic potential (see section 8.2.1 for a brief summary of the pitchfork bifurcation). The analysis of chapter 8 showed that bifurcations to time-dependent states (such as traveling waves) are typically non-potential. We now consider an example of this in active matter, in which nonreciprocal interactions lead to time-dependent phases that spontaneously break parity (mirror symmetry).[31]

9.8.1 Chiral phases in nonreciprocal active matter

We can illustrate the main features of nonreciprocal active matter with the following model:

$$\partial_t \theta_m = \omega_m + \sum_n J_{mn} \sin(\theta_n - \theta_m) + \eta_m(t), \tag{9.63}$$

which can be thought of as a simple extension of the Vicsek model. When the agents are at *fixed* positions, this model is known as the

Kuramoto model, which was introduced to study the synchronization of coupled oscillators with phase angles θ_m. It qualitatively describes the collective behavior of clocks ticking, neurons firing, or fireflies flashing.[32] With strong enough coupling, a synchronized state emerges where all oscillators evolve in phase with the same frequency.

In our case, the variable θ_m describe the angle in the plane of the velocities with which the agents move, so that the positions $\vec{r}_m$ in the plane are given by

$$\partial_t \vec{r}_m = v_0 \begin{pmatrix} \cos\theta_m \\ \sin\theta_m \end{pmatrix}. \tag{9.64}$$

An agent m tends to align with an agent n when $J_{mn} > 0$, or to antialign when $J_{mn} < 0$. The standard Vicsek flocking model corresponds to $J_{mn} > 0$. In the absence of interactions and noise the agents all rotate independently with their own frequency ω_m. For positive J_{mn}, there is a critical coupling at which a transition takes place, from incoherent rotations or motion to synchronized rotation (when the positions are fixed while $\omega_m \neq 0$) or to flocking when the particles move according to equation (9.64).

Now consider two copies of the Vicsek model describing two species, labeled 1 and 2. Without interaction between the two species, each has its own order parameter (average velocity) describing the flocking. The behavior of the model becomes especially interesting, however, when there are interactions between the species. When the interactions are reciprocal, $J_{12} = J_{21}$, we find, in addition to a disordered phase, two *static* phases where $\vec{v}_1$ and $\vec{v}_2$ are (anti)aligned, in analogy with (anti)ferromagnetism. When the interactions are nonreciprocal, $J_{12} \neq J_{21}$, a time-dependent chiral phase with no equilibrium analogue emerges between the static phases. In this chiral phase, parity is spontaneously broken: $\vec{v}_1$ and $\vec{v}_2$ (the two species are represented in red and blue in figure 9.17) rotate with a fixed relative angle $\Delta\phi$, either clockwise or counterclockwise, at a constant rotation rate $\Omega_{\text{ss}} \equiv \partial_t \bar{\phi}$, where $\bar{\phi}$ is the angle between $(\vec{v}_1 + \vec{v}_2)/2$ and a fixed direction. The chiral phase is caused by the frustration experienced by agents with opposite goals: species 1 (red) wants to align with species 2 (blue) but not vice versa. This dynamical frustration results in a 'chase and run away' motion of the order parameters $\vec{v}_1$ and $\vec{v}_2$.

Interestingly, Rayleigh-Bénard convection in rotating cells is described by a nonreciprocal model, in which the nonreciprocal effects affect the nonlinear terms describing mode interactions. See the note in the margin of equation (8.54).

Figure 9.17 illustrates the aligned-to-chiral transition in flocking as well as in synchronization and pattern formation.[33] The bottom row of the figure illustrates a strong link with the formation of patterns as discussed in chapter 8: in pattern-forming non-equilibrium systems, nonreciprocal interactions can similarly lead to a transition from stationary to moving patterns, and the methods of the theory of pattern formation and dynamical systems can be used to understand general features of the phases and phase transitions.

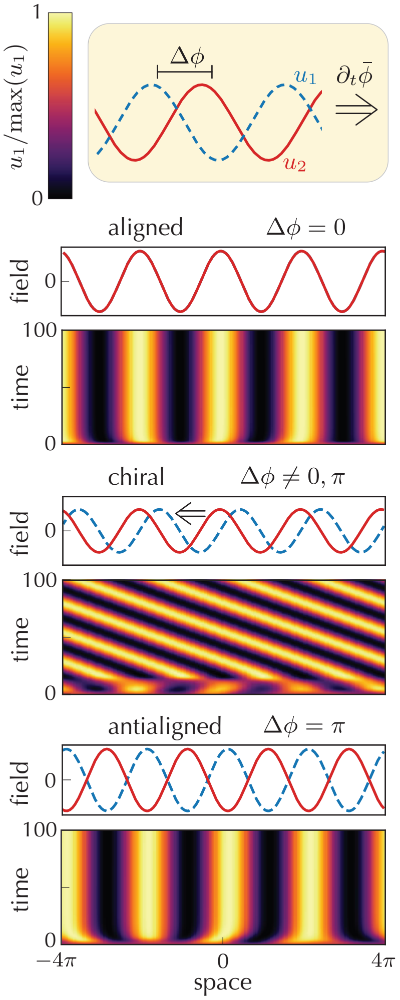

Figure 9.18. Space-time density plots of the field $u_2(x,t)$ shown with snapshots of the fields $u_1(x,t)$ and $u_2(x,t)$ at the top. In the chiral phase with a finite phase difference $\Delta\phi$, the patterns move at constant velocity, either to the left or to the right (spontaneously breaking parity). In the antialigned case $\Delta\phi = \pi$, the patterns are stationary again. Image courtesy of Michel Fruchart.

In problem 9.6, you will show explicitly how the amplitude equations reduce to (9.67)–(9.68) and derive the explicit expressions for the coefficients $\alpha = 2[\epsilon_-^2 - \epsilon_+\epsilon_0]/\epsilon_0$ and $\gamma = 2\epsilon_-$. Note also that we have expanded in these equations the right-hand sides in $\Delta\phi$, to bring out the bifurcation structure of (9.67). The full equations are periodic in $\Delta\phi$. This reflects the fact that when one of the patterns is shifted by one wavelength relative to the other, the pattern does not change.

To illustrate the cross-fertilization of the two fields, we will show below how such transitions can be studied with the methods developed in chapter 8.

9.8.2 Nonreciprocal pattern formation: A case study

Let us start by considering a classic model of pattern formation that we already encountered in section 8.2.2, the Swift-Hohenberg model, as it is the simplest type of spatiotemporal model that exhibits finite wavelength periodic patterns. We generalize to two fields u_1 and u_2 obeying a set of two Swift-Hohenberg equations with nonreciprocal interactions, namely

$$\partial_t u_i = \epsilon_{ij} u_j - (1+\nabla^2)^2 u_i - g u_i^3, \tag{9.65}$$

where we have introduced the nonsymmetric coupling matrix $\epsilon_{12} \neq \epsilon_{21}$. Unlike the standard Swift-Hohenberg model that can be derived from a potential, the nonreciprocal ones cannot.

Following the amplitude equations approach developed in the chapter on pattern formation (see section 8.5), we can write $u_i(x) = A_i(x)e^{ik_c x} + \text{c.c.}$, where k_c is the critical wavevector where the instability sets in (here $k_c = 1$). Note that shifting the phase of the amplitude A_i by $\delta\phi$ ($A_i \to A_i e^{i\delta\phi}$) amounts to a translation of the periodic one-dimensional pattern $u_i(x,t)$ by a distance equal to $\delta\phi/k_c$ (see section 8.5.2.d.) Using the symmetry considerations discussed in the previous chapter (or a full-length explicit derivation), the set of nonreciprocal Swift-Hohenberg equations reduces, just above the instability threshold, to the following set of nonreciprocally coupled amplitude equations:

$$\begin{aligned} \partial_t A_1 &= \epsilon_0 A_1 + \epsilon_{12} A_2 - g|A_1|^2 A_1, \\ \partial_t A_2 &= \epsilon_0 A_2 + \epsilon_{21} A_1 - g|A_2|^2 A_2, \end{aligned} \tag{9.66}$$

where we have introduced the nonsymmetric coupling among the amplitudes $\epsilon_{12} = \epsilon_+ + \epsilon_-$ and $\epsilon_{21} = \epsilon_+ - \epsilon_-$, and ignored the gradient terms.

We now write the two complex amplitudes (that act as order parameters in this pattern formation problem) as $A_i = a_i e^{i\phi_i}$ ($a_i = |A_i|$) and assume that the two fields are primarily coupled antisymmetrically, so that $\epsilon_0 \gg \epsilon_- \gg \epsilon_+$. The amplitude equations reduce to

$$\partial_t \Delta\phi = \alpha\Delta\phi - \beta\Delta\phi^3, \qquad (\beta > 0) \tag{9.67}$$

$$\partial_t \bar{\phi} = \gamma\Delta\phi, \tag{9.68}$$

where $\Delta\phi = \phi_2 - \phi_1$ and $\bar{\phi} = \phi_2 + \phi_1$. The stationary state of the first equation is $\Delta\phi = 0$ if $\alpha < 0$ and $\Delta\phi = \pm\sqrt{\alpha/\beta}$ if $\alpha > 0$. The case $\alpha < 0$ results in two *static* patterns that are completely in phase, while the case $\alpha > 0$ with $\Delta\phi \neq 0$ corresponds to two periodic patterns offset by a constant phase difference $\Delta\phi$ both *moving* (because the sum of their phases increases indefinitely) at a speed proportional to $\gamma\Delta\phi$, as illustrated in figure 9.18. The resulting phase diagram from this perturbative analysis is shown in figure 9.19, while figure 9.20.a shows the full phase diagram. By itself, equation (9.67) represents a standard pitchfork bifurcation, but in conjunction with equation (9.68) it forms a system of dynamical equations that cannot be expressed in terms of the gradient of a potential, and that describes a class of bifurcations known as parity-breaking bifurcations or drift instabilities.[34]

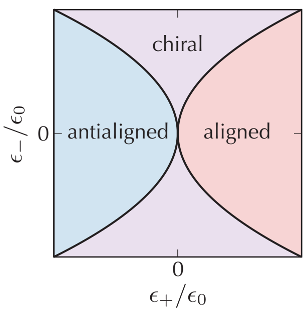

Figure 9.19. The perturbative phase diagram of the exceptional transition computed in the main text and problem 9.6 as a function of the ratios ϵ_-/ϵ_0 and ϵ_+/ϵ_0.[35]

This pattern formation problem exemplifies a transition from a state described by static order parameters to a non-equilibrium steady state described by time-varying order parameters.

See section 8.2.1 for an introduction to the pitchfork bifurcation.

9.8.3 Exceptional points and parity-breaking bifurcations

To understand the mechanism underlying the transition, we linearize the above equations about $\Delta\phi = 0$ and an arbitrary fixed $\bar{\phi}$, to obtain

$$\partial_t \begin{pmatrix} \Delta\phi \\ \bar{\phi} \end{pmatrix} = \begin{pmatrix} \alpha & 0 \\ \gamma & 0 \end{pmatrix} \begin{pmatrix} \Delta\phi \\ \bar{\phi} \end{pmatrix}. \tag{9.69}$$

See problem 9.10 for an explicit derivation of these equations. The matrix in (9.69) is called a Jacobian. Generally, the Jacobian of a vector field is the matrix of its derivatives.

At the transition point $\alpha = 0$, the matrix on the right-hand side is not diagonalizable since it has two eigenvalues equal to zero; at that point

$$\partial_t \begin{pmatrix} \Delta\phi \\ \bar{\phi} \end{pmatrix} = \gamma \begin{pmatrix} 0 & 0 \\ 1 & 0 \end{pmatrix} \begin{pmatrix} \Delta\phi \\ \bar{\phi} \end{pmatrix}. \tag{9.70}$$

While we have derived equations (9.67), (9.68), and (9.70) in the context of a specific example, they apply more generally to non-reciprocal phase transitions in various systems. For instance, nonreciprocal flocking can be analyzed in the same way by considering two Toner-Tu equations (section 9.2.3) with asymmetric couplings.

The point where two eigenvalues of a matrix vanish is called an exceptional point of the matrixes and it is characteristic of nonreciprocal phase transitions.

In the Jacobian matrix above, one eigenvalue always vanishes because it corresponds to translation invariance of the pattern (and to rotation invariance of the $\vec{v}_i$ in the flocking model): it is known as the Goldstone mode of broken translation (or rotation) invariance, as indicated by the green line in figure 9.20.b. At the bifurcation, the remaining eigenmode (orange line in the figure) coalesces with the Goldstone mode (green line) at exceptional points, in red. In addition to having the same eigenvalue (zero), the two eigenmodes become parallel at this point.

The same approach applies to order parameters associated with conservation laws, e.g., continuum mechanics models with odd-elasticity and odd-viscosity that conserve linear momentum (see previous sections) and nonreciprocal models of phase separation that conserve mass, discussed for example by You et al., 2020 and Saha et al., 2020. In all these problems one obtains (nonlinear) diffusion-like equations with additional diffusion coefficients accounting for nonreciprocal couplings between the components of the relevant fields as illustrated in (9.51).

The structure of exceptional points leads to a pictorial description of the phase transition to the chiral phase. Let us represent the order parameter as a ball constantly kicked by noise at the bottom of a wine bottle–shaped potential. Because of the nonreciprocal couplings, there are transverse nonconservative forces in addition

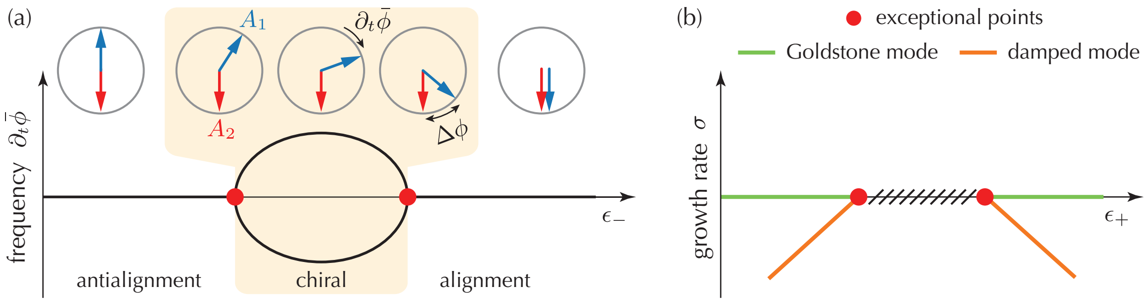

Figure 9.20. (a) Schematic bifurcation diagram of the exceptional transition for two coupled vector models (9.63), showing the frequency of the steady state $\Omega_{ss} \equiv \partial_t\bar{\phi}$. Between the static (anti)aligned phases with $\Omega_{ss} = 0$, an intermediate chiral phase spontaneously breaks parity. Two equivalent steady states (clockwise and counterclockwise, corresponding to opposite values of Ω_{ss}) are present in this time-dependent phase. The chiral phase continuously interpolates between the antialigned and aligned phases, both through $|\Omega_{ss}|$ and the angle between the order parameters $\vec{v}_A$ and $\vec{v}_B$. (b) The transition between (anti)aligned and chiral phases occurs through the coalescence of a damped (orange) and a Goldstone mode (green) at an exceptional point (red dot). Adapted from Fruchart et al., 2021.

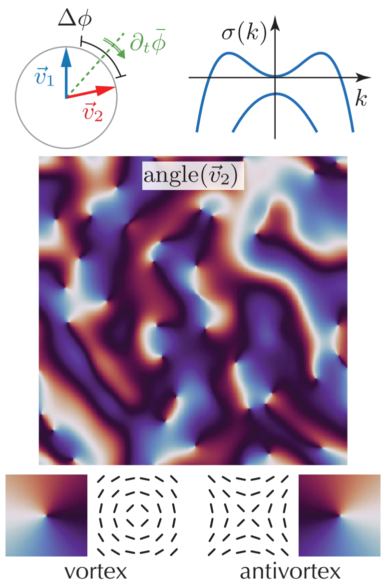

Figure 9.21. As explained in the text, a type II instability discussed in section 8.6 occurs near exceptional points. We consider here nonreciprocal flocking (top left), where the two velocity vectors rotate at a constant speed while keeping their relative orientation fixed. The growth rate of perturbations (top right) is shown signaling a finite momentum instability. The middle panel shows a snapshot of the phase angle of one of the velocities in two-dimensional hydrodynamic simulations in the unstable regime: the resulting chaotic pattern is dominated by vortices and antivortices (bottom panel). In time-dependent simulations these are found to constantly annihilate and unbind. Adapted from Fruchart et al., 2021.

to the potential energy landscape. When you kick the ball uphill, it moves perpendicular to the direction of the height gradient along the bottom of the potential, but a kick in the direction along the bottom does not drive the ball up the gradient. This arises because of the non-orthogonality of the eigenmodes of the Jacobian near the exceptional point. At the exceptional point, the ball moves only along the bottom of the potential, irrespective of how it is kicked: this is the onset of the chiral phase.

9.8.4 Exceptional points-induced instabilities

In a spatially extended system, one has to consider gradient terms in the field theory. These depend on the physical system under consideration: for instance, there can be convective terms in nonreciprocal flocking, which would be absent in nonreciprocal magnets. Let us therefore consider the generic equation of motion,

$$\partial_t \begin{pmatrix} \Delta\phi \\ \bar{\phi} \end{pmatrix} = \left[\begin{pmatrix} 0 & 0 \\ 1 & 0 \end{pmatrix} + M\vec{v}_0 \cdot \vec{\nabla} + N\nabla^2 \right] \begin{pmatrix} \Delta\phi \\ \bar{\phi} \end{pmatrix}, \tag{9.71}$$

where M and N are 2×2 matrices that are not necessarily symmetric. Equation (9.71) is obtained by including gradient terms in equation (9.66) and repeating the analysis, leading to (9.70).

In problem 9.11, you will take a Fourier transform and diagonalize the matrix equation to obtain the complex growth rates $\sigma(k)$. When $\sigma(k) > 0$ with a maximum at finite k, a type II instability is triggered, following the classification scheme introduced in the previous chapter—compare figure 8.14 to the spectrum in figure 9.21 (top panel, right). Equation (9.71) with $M = 0$ describes the soft modes of the Kuramoto-Sivashinsky equation discussed in section 8.6.[36] As the lower panels of figure 9.21 illustrate, in the case of nonreciprocal flocking the non-equilibrium steady state is characterized by continuous unbinding and annihilation of vortices and antivortices in the vector order parameters, reminiscent of active nematic turbulence.

9.9 Applications to biological problems

While the study of active matter was initially stimulated by problems in the life sciences, the field is now increasingly having an impact on these disciplines, as the methods and insights which have been developed throw new light on biological problems. We close this chapter by sketching some examples of the avenues which are opening up. As we shall see, insights from non-equilibrium pattern formation and active matter often go hand in hand here.

9.9.1 Active gels

An active gel is a material composed of a network of crosslinked biopolymer filaments and molecular motors, as illustrated in figure 9.22. These active media are driven out of equilibrium by two distinct phenomena: the action of the molecular motors on the filaments and the spontaneous polymerization and depolymerization of the monomers within each filament. Both behaviors are energy transduction mechanisms which generate mechanical work from chemical energy. The relevant hydrodynamic theory reflects the complexity of the system, but in schematic form it can be rationalized by putting together key equations we already encountered in our treatment of (passive) polymer viscoelasticity, polar and active nematic fluids, and intuitive symmetry-based reasoning.

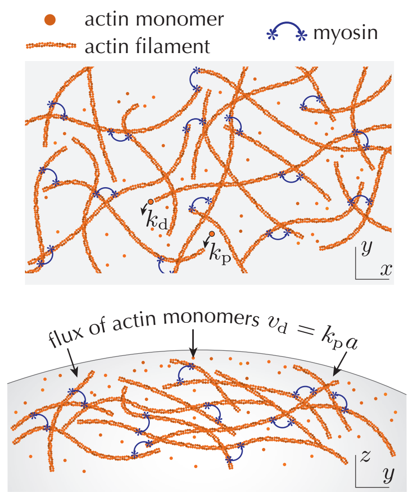

Figure 9.22. Schematic picture of an active gel composed of actin filaments and myosin motors which crosslink these filaments. The polymerization processes with rate constant k_p and depolarization processes with rate constant k_d are indicated.

a. Modeling of active gels

To model active gels at the hydrodynamic level we identify the relevant conserved quantities: the overall mass, the number of monomers, the number of motors and momentum. Thus, the hydrodynamic equations will describe how the densities of these conserved quantities evolve. Since the filaments are on average parallel to each other, we need to include an additional broken-symmetry variable that describes their local orientation. Depending on whether there is nematic or polar order, this will be the director $\hat{n}$ or the polarization vector $\vec{p}$, respectively. The relevant hydrodynamic equations were already written in section 9.5.1 for active nematics.

The momentum equation includes a total stress tensor given by

$$\sigma_{ij} = \sigma_{ij}^{\text{vis}} + \sigma_{ij}^{\text{el}} + \sigma_{ij}^{\text{a}}. \tag{9.72}$$